Journal of ELECTRONIC MATERIALS, Vol. 48, No. 7, 2019
https://doi.org/10.1007/s11664-019-07225-3

Flexoelectric Effects in Corrugated Boron Nitride Nanoribbons

FARZANEH SHAYEGANFAR,[1,2,5] ZIBA TORKASHVAND,[2] KAVOOS MIRABBASZADEH,[2] and ROUZBEH SHAHSAVARI[1,3,4,6]

1.—Department of Civil and Environmental Engineering, Rice University, Houston, TX 77005, USA. 2.—Department of Energy Engineering and Physics, Amirkabir University of Technology, Tehran, Iran. 3.—Smalley Institute for Nanoscale Science and Technology, Rice University, Houston, TX 77005, USA. 4.—C-Crete Technologies LLC, Stafford, TX 77477, USA. 5.—e-mail: fs24@rice.edu. 6.—e-mail: rouzbeh@rice.edu

Hexagonal boron nitride (h-BN) monolayer is an isostructural analogue to graphene and promising dielectric. Inspired by recent experimental reports, we focus on suspended and corrugated boron nitride nanoribbons (BNRs) as model systems, and report an intriguing flexoelectric polar effect using a series of *ab initio*-based density functional theory and tight binding calculations. Our results decode various synergies of the complex flexoelectrical properties including the role of corrugation height, structural deformation, and orbital mixing in corrugated BNRs. We demonstrate structural deformation of BNRs significantly contribute to the magnitude of electric dipole moment and bandgap closing, converting the insulating BNRs to semiconductors. This important finding, combined with the fundamental insights into the nature of electromechanical coupling, provides key hypotheses for design and modulation of novel nanoelectronic and nanophotonic devices.

Key words: Flexoelectricity, corrugated BN, *ab initio*, polarization

INTRODUCTION

Flexoelectricity is an electromechanical property of a dielectric material whereby it generates a voltage in response to strain gradient and exhibits an induced electrical polarization.[1–3] Flexoelectric effect is usually small in bulk three-dimensional (3D) solids, and evades experimental detection unless large strain gradients are externally imposed or artificially designed inhomogeneous metamaterials are used.[4,5] Contrary to 3D systems, two dimensional (2D) nanocrystals such as graphene and hexagonal boron nitride (h-BN) sustain large elastic structural distortions and exhibit unusual forms of electromechanical coupling. For instance, the BN sheet becomes pyroelectric when it is wrapped into a chiral or a zigzag nanotube with a macroscopic polarization (quadratic flexoelectric effect).[6,7] 2D boron based nanosheets possess electronic properties, offering the lightest catalyst for hydrogen and oxygen evolution reaction.[8]

The h-BN sheet has remarkable thermal stability (air-stable up to 1000°C),[9,10] exceptional hardness and mechanical strength,[11] and chemical stability,[12,13] which is suitable for fabricating devices, and tolerating harsh environments.[14] Mechanical properties of monolayer boron pnictides (BX, X ¼ N, P, As, and Sb) show that they are stable under biaxial strain smaller than 18%.[15] One-dimensional (1D) BN derivative, BN nanoribbons (BNRs), can be obtained by cutting an h-BN sheet or unzipping a BN nanotube.[16] More recently, a new allotrope of BN, i.e., haeckelite structures with octagonal and square rings, has been studied by Roondhe et al.,[17] revealing the significant electronic properties applicable in sensing biomolecules as a biosensor. For instance, the interaction of BN nanostructures with alkaloids (caffeine and nicotine) suggests a precise biosensor based on BN nanomaterials.[18] Lopez-Bezanilla et al.[19] studied the electronic and magnetic properties of O- and S-functionalized BNRs, indicating metallicity.

(Received December 12, 2018; accepted April 12, 2019; published online April 29, 2019)

BNRs have attracted increasing attention because of transverse electric polarization,[20,21] leading to piezoelectric effects[22] and half-metallic interfaces with graphene ribbons.[23–25] Hydrogenated side-by-side aligned BNRs will have a considerable Coulomb interaction in addition to the van der Waals interaction at the nanoscale interfaces. This substantial interface interaction may afford the formation of stable BN superstructures with different properties.[26]

The mechanical properties of the h-BN films reported by Song et al.[27] show a 2D elastic modulus in the range of 200–500 N/m, measured by nanoindentation.[27] They used circular wells with diameter around 1 μm which were patterned onto a silicon substrate by e-beam lithography and reactive ion etching (RIE) techniques.[27] A noncontact-mode atomic force microscopy (AFM) test was used to obtain the stress and strain applied by indenting the center of each freestanding membrane with a diamond tip.[27] Inspired by these experimental data, our goal is to study the variation of structural and electronic properties induced by distortion and corrugated BNRs with respect to pure BNRs. Using a series of first-principles calculations and tight-binding (TB) approach, we show that the corrugated BNRs can indeed be polarized via considerable structural deformation and undergo a transition from an insulator to a semiconductor with increasing indentation depth of BNRs. These results are robust against variations in nanocomposites, and delineate the general significance of polar nanostructures to achieve a tunable polarization toward developing nanoelectronic devices.

COMPUTATIONAL METHODS

Tight-Binding (TB) Model and Green's Function

BNRs not only follow the structure of graphene nanoribbons (GRs), as they consist of two different types of sublattices, A and B, but also appear in two different types of atoms, boron and nitrogen, as illustrated in Fig. 1. For such a system, we model π and π^* band energy dispersion employing a simple nearest-neighbor TB parameterization. In this way, the wave function of A (B) sublattice can be shown as[28,29]:

$$\left|\psi_{A(B)}\right\rangle = \frac{1}{N_{A(B)}}\sum_{i=1}^{n}\sum_{x_{A_i(B_i)}} e^{ik_x.x_{A_i(B_i)}}\phi_{A(B)}(i)|A_i(B_i)\rangle \quad (1)$$

where $\phi_{A(B)}(i)$ is the component for A (B) sublattice in the y direction, which is perpendicular to the edge. For BNRs with solid boundaries (considering hard-wall boundary condition by Zheng et al.[29]), the transverse wave vector q is introduced as: $q_y = \frac{2}{\sqrt{3}a}\frac{p\pi}{n+1}, \quad p = 1, 2, \ldots, n.$

After constructing the wave function for our system, we now focus on the Hamiltonian. We start

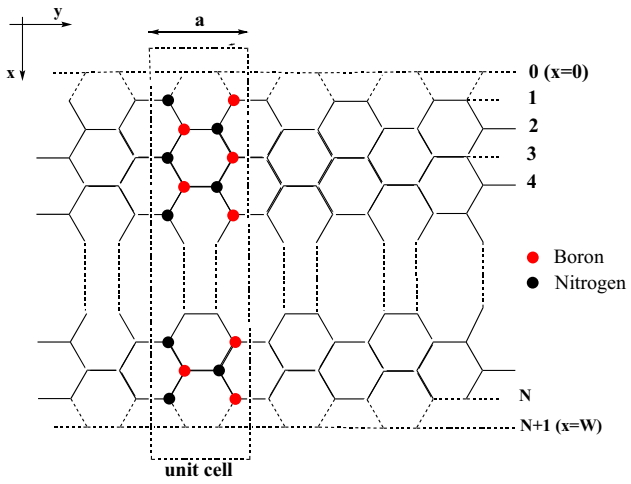

Fig. 1. Structure of BN nanoribbons (BNRs). The dashed rectangle shows the unit cell, a = 2.5 Å is lattice constant from Ref. 24 and N defines the ribbon width.

with the case of interaction between equivalent atoms (belonging to the same sub-lattice). We have:

$$\begin{aligned} H_{AA} &= \frac{1}{N}\sum_{R_A}\sum_{R_{A'}} e^{ik(R_{A'}-R_A)}\langle\phi_A(r-R_A)|H|\phi_A(r-R_{A'})\rangle \\ &= \frac{1}{N}\sum_{R_A}\langle\phi_A(r-R_A)|H|\phi_A(r-R_A)\rangle = \varepsilon_{p_z} \end{aligned} \quad (2)$$

where N is the number of unit cells, and R_A and $R_{A'}$ are the position of atoms A and A'. ε_{p_z} describes the energies of electrons on the $2p_z$ orbitals. By keeping just three nearest neighbors in mind along with interaction between electrons bound to nonequivalent atoms and using the fact that there is translational invariance in a Bravais lattice, the sum over each atom of a sub-lattice is done N times and therefore Eq. 2 becomes:

$$\begin{aligned} H_{AB} &= \frac{1}{N}\sum_{R_A}\sum_{R_B} e^{ik(R_B-R_A)}\langle\phi_A(r-R_A)|H\,|\phi_B(r-R_B)\rangle \\ &= \gamma\left(e^{ikR_{11}} + e^{ikR_{12}} + e^{ikR_{13}}\right) \end{aligned} \quad (3)$$

where γ denotes the hopping parameter and R_{1i} are distances between an atom and its three nearest neighbors. By defining the function $f(k)$ and taking into account the three mentioned distances we have: $f(k) = e^{ikR_{11}} + e^{ikR_{12}} + e^{ikR_{13}} = e^{-\frac{iak_x}{\sqrt{3}}} + 2e^{\frac{iak_x}{2\sqrt{3}}}\cos\left(\frac{a}{2}q\right)$, in which the mentioned transverse wave function is held. The matrix form of the Hamiltonian is ready with all provided parameters as:

$$H = \begin{pmatrix} \varepsilon_b & \gamma f(k) \\ \gamma f(k)^* & \varepsilon_n \end{pmatrix} \quad (4)$$

where ε_b and ε_n are the on-site energies at boron and nitrogen sites. The eigenvalues of Hamiltonian H

(Eq. 4), are given by: $E = E_0 \pm \frac{1}{2}\sqrt{E_g^2 + 4|f|^2}$, where $E_0 = \frac{\varepsilon_b + \varepsilon_n}{2}$ and $E_g = \varepsilon_b - \varepsilon_n$ is the band gap. Here, $\pm$ denotes the conduction and valance bands, respectively. Figure 2a shows the energy dispersion for BNRs with width $N = 7$. For this, we set on-site energies $\varepsilon_b = 0.0$ eV and $\varepsilon_n = -4.57$ eV, and also hopping parameter $\gamma = 1.95$ eV from earlier reports[30,31] with a little change to adjust the Fermi level. The density of states (DOS) is plotted in Fig. 2b, while the computational details of the DOS using Green's function are given in the Appendix.

DFT Computational Methods

All the structural optimization and electronic calculations are performed within the framework of density functional theory (DFT) as implemented in the VASP code. A number of calculations, such as the Kohn–Sham equation, are performed based on a projector-augmented wave approach with a plane wave basis set. The electronic self-consistent field (SCF) is converged to 10^{-5} eV per cell.[32–34] A generalized gradient approximation (GGA) of the Perdew–Burke–Ernzerhof (PBE) functional is employed for the exchange correlation potential.[35]

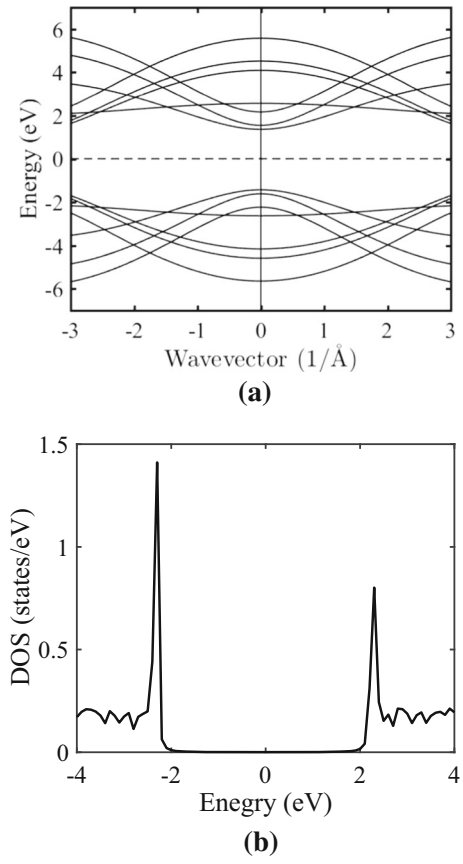

Fig. 2. (a) Electronic band structure $E(k)$ of BNR of width $N = 7$, (b) density of states (DOS) of BNR of width $N = 7$.

The BNRs are modeled by a supercell as shown in Fig. 4a, with a vacuum of 50 Å.

BNRs are modeled within a supercell as shown in Figs. 4 and 6 with at least 30 Å of vacuum (non-interacting cells), which contains 48 BN atoms. All configurations are relaxed with a force tolerance of 0.01 eV/Å. The geometry optimization was pursued until the convergence criterion was less than 10^{-5} eV for total energy and less than 0.01 eV/Å for forces and with maximum stress of 0.02 GPa. We adopt a fine $70 \times 1 \times 1$ Monkhorst–Pack k-points grid for sampling of the Brillouin zone, and cutoff of 300 Ry for numerical integrals in a real space.

We tested several cutoff and K-points sampling for flat and distorted BNRs, getting the precise data. We modeled the flat armchair BNRs by the supercell shown in Fig. 4a, which contains 48 BN atoms (24 B atoms, and 24 N atoms). Moreover, we modeled the suspended BNRs and sine-wave distortion BNRs with different indentation depth (h) as shown in Figs. 4 and 6. During the geometry optimization, the boundary of BN was kept frozen in the $\boldsymbol{y}$ direction, and was periodic in the x direction. In order to evaluate the influence of boundary condition (BC) constraints on the dipole moment of BN, we have also considered the flake BN (non-periodic BN), to compare with BNRs.

For first-principle phonon calculation, we have applied the force constant method, and we constructed the dynamical matrix and diagonalized, acquiring all phonon modes. Dynamical matrices are computed in a larger supercell (168 atoms) and 12 wave vectors in the irreducible wedge of BZ.[36]

RESULTS AND DISCUSSION

We have investigated two structures (suspended and sine-wave distortion) shown in Figs. 4 and 6, respectively, with different indentation depth (h). Our study begins with investigation of the stability of BNRs by using the phonon spectrum, indicating dynamical behaviors. We plotted the phonon dispersion curves for suspended BNRs with different indentation depths: $\delta = 1.0$ Å, 2.0 Å, and 3.0 Å in Fig. 3. This figure reveals that all phonon modes are real and positive, confirming the stability of BNR configurations.

The electronic properties of suspended BNRs of DFT data are reported in Table I in terms of electrical dipole moment vector, $P = (p_x, p_y, p_z)$, band gap energy, E_g, and optimized indentation height (h') for different loaded structures as shown in Fig. 4a, b, c and d (top panel).

The trends observed in Table I are: (1) dipole moment vector has in-plane and out-plane components, (2) increasing the distance associated with the indentation height of BNRs increases the in-plane and out-of-plane component of the dipole moment; e.g., $p_z = 0$ Debye at $h = 0$ Å goes to -1.32 Debye at $h = 3$ Å, (3) bandgap energy (E_g) closes

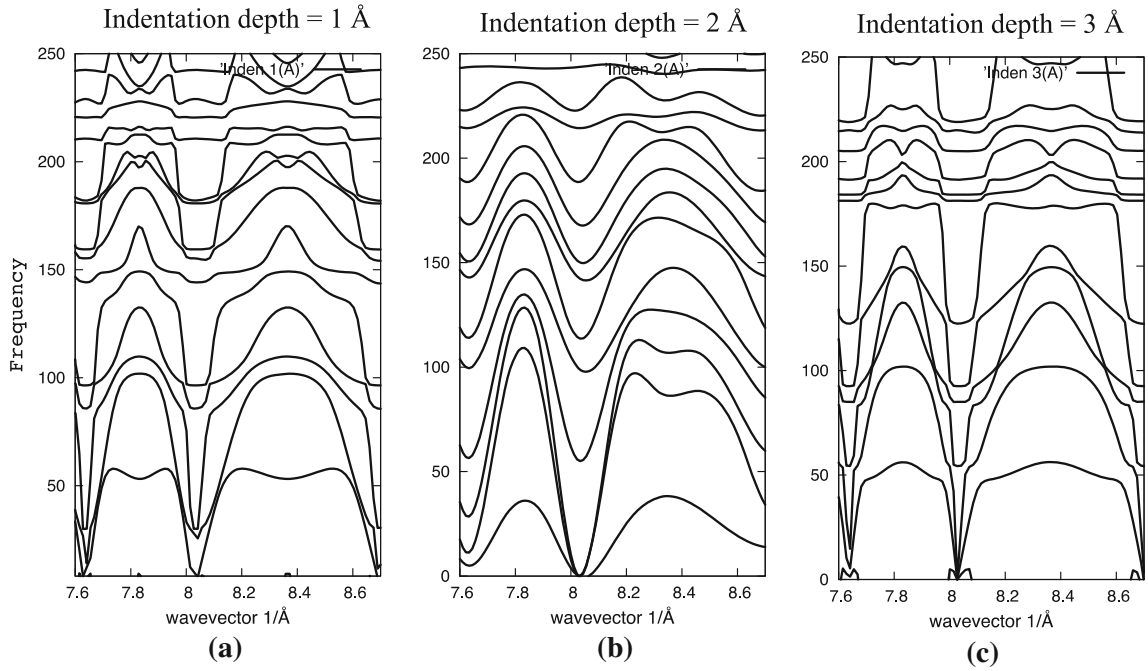

Fig. 3. Phonon spectrum for suspended BNRs: (a–c) with indentation depth δ = 1.0 Å, 2.0 Å, and 3.0 Å.

Table I. Dipole moment (P), band gap energy (E_g) and optimized indentation height (h') for different suspended BNRs

	P (p_x, p_y, p_z) (Debye)	E_g (eV)	h'_{opt} (Å)
Indentation depth			
0 Å	(0, −1.22, 0)	4.21	0
1 Å	(0, −1.32, −0.37)	3.83	0.87
2 Å	(0, 1.58, −0.75)	3.57	1.85
3 Å	(0, −2.15, −1.32)	3.34	2.80

with increasing indentation height; i.e., at h = 0 Å, the E_g = 4.2 eV and at h = 3 Å, the E_g = 3.3 eV.

Figure 4 also demonstrates the calculated electronic band structure and the variation of the total DOS as a function of the DFT energy, providing additional details on the electronic effects of polarized BN. The calculated band structures and DOS for a perfect BNR is in close agreement with the TB and Green's function approach, which is presented in Fig. 2. In view of Fig. 4, we observe that indentation perturbs significantly the electronic states of BN in the vicinity of the Fermi level. Specifically, there is a gradual displacement of the valence band (VB) and conduction band (CB) toward the Fermi level region with increasing the indentation depth. This energy shift suggests an improved electron cloud overlap as BN polarization increases, which is also supported by the gap energy reported in Table I. Hence, the calculated variations in the VB and CB lead to a band gap closing from 4.21 eV to 3.34 eV as h increases from 0 Å to 3 Å. The structural deformation of BN is consistent with improved system polarization, which maximizes orbital mixing and, as a consequence, band gap closing. This polarization originates from different electronegativity of B and N atoms and embodies an inbuilt electric field.

In order to compare the structural and electronic properties of suspended BNRs with sine-wave distorted shapes as plotted in Fig. 6 (top panels), we performed phonon calculation and DFT computation for sine-wave BNRs. Figure 5 shows the phonon spectrum for sine-wave BNRs with indentation depth δ = 1.0 Å, 1.5 Å, and 2.0 Å. Phonon dispersion curves as a key parameter for crystal stability indicate that all phonon modes are positive, then sine-wave BNRs are stable.

Table II presents DFT data for optimized structural parameters for sine-wave corrugated BNRs. Akin to Table I, the following trend holds here as well: (1) the dipole moment vector has in-plane and out-of-plane components, (2) increasing indentation height of BNRs increases the dipole moment; (3) E_g closes with increasing indentation height.

The gap reduction in the BNRs can be understood by analyzing the electronic structures. A central question is what is the source of band gap closing in corrugated BNRs? To answer this question, we

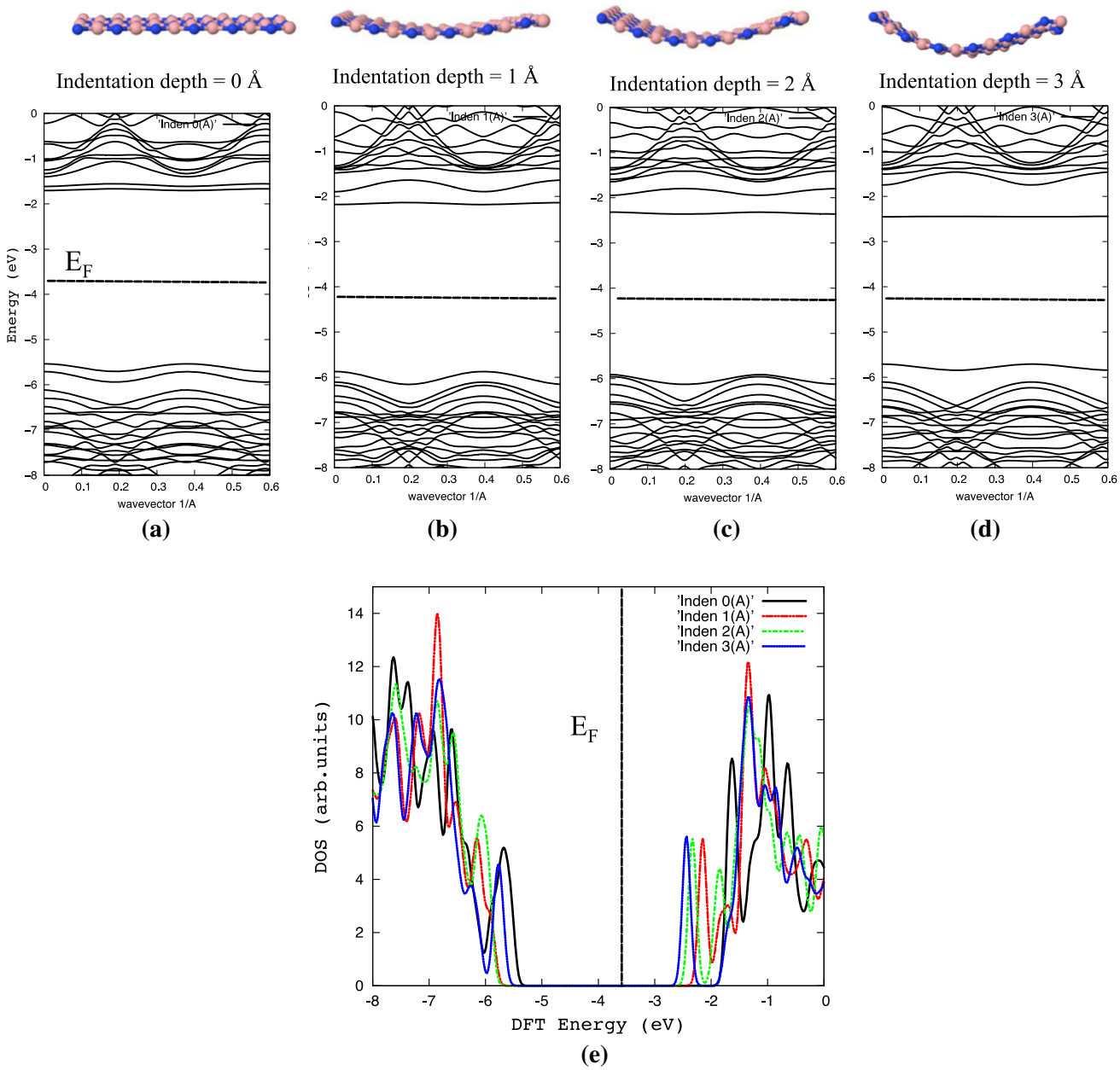

Fig. 4. The deformation sequence for suspended BNRs: (a) flat (unloaded) structure, (b–d) with indentation depth δ = 1.0 Å, 2.0 and Å, 3.0 Å; the middle panel shows their electronic band structure for BNRs. (e) Total density of states (DOS) for the loaded structure with indentation depth of 1.0 Å, 2.0 Å, and 3.0 Å compared with a flat structure.

examined the profile of electronic band structure of corrugated BNRs in Fig. 6. Flat bands in the CB indicate localized density of electrons, giving a polar character in these structures and band gap reduction as reported by previous study.[26] In order to evaluate the influence of structural BC constrains on the polarization of the corrugated BNRs, we have also considered the corrugated BN flakes, which allow us to obtain a polarization trend comparable with BNRs (periodic structures). The polarization of BN flakes increases rapidly with increasing indentation depth as shown in Fig. 7. This figure shows that the polarization strongly depends on the indentation depth of the nanostructure. The impact of the BN flakes is more significant since the structural deformation is increased.

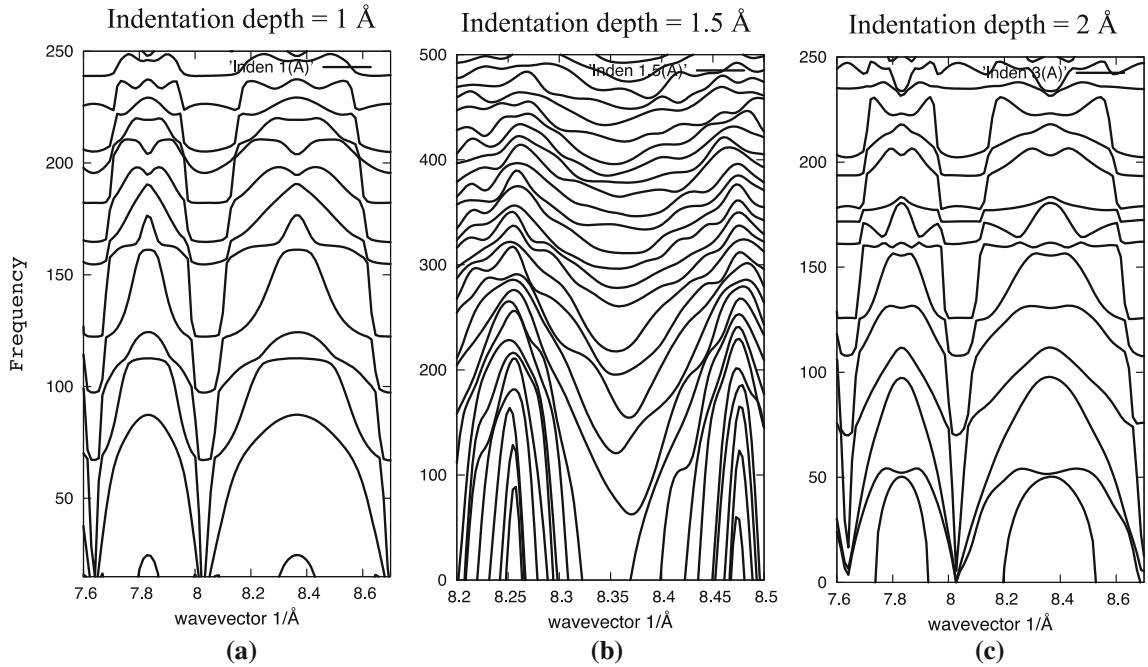

Fig. 5. Phonon spectrum for sine-wave distortion of BNRs: (a–c) with indentation depth δ = 1.0 Å, 1.5 Å, and 2.0 Å.

Table II. Dipole moment (P), band gap energy (E_g) and optimized indentation height (h') for different sine-wave distorted BNRs

	P (p_x, p_y, p_z) (Debye)	E_g (eV)	h'_{opt} (Å)
Indentation depth			
0 Å	(0, −1.22, 0)	4.21	0
1 Å	(0, 1.81, 0.45)	3.88	0.66
1.5 Å	(0, −2.27, 0.39)	3.79	0.92
2 Å	(0, 4.41, 0.92)	3.02	1.35

CONCLUSION

Our comprehensive first-principles calculations have shown that the band gap of corrugated BNRs can be reduced upon structural deformation. The distorted and corrugated BNRs change from an insulator to a semiconductor with increasing indentation depths of BNRs. This electronic phase transition, which entails increasing the electrical dipole moment, stems from polarizations at the bond distortion of BNRs. Our results suggest that structural deformation and corrugation for a group of semiconducting composite nanostructures could be used to tune and control the polarization and

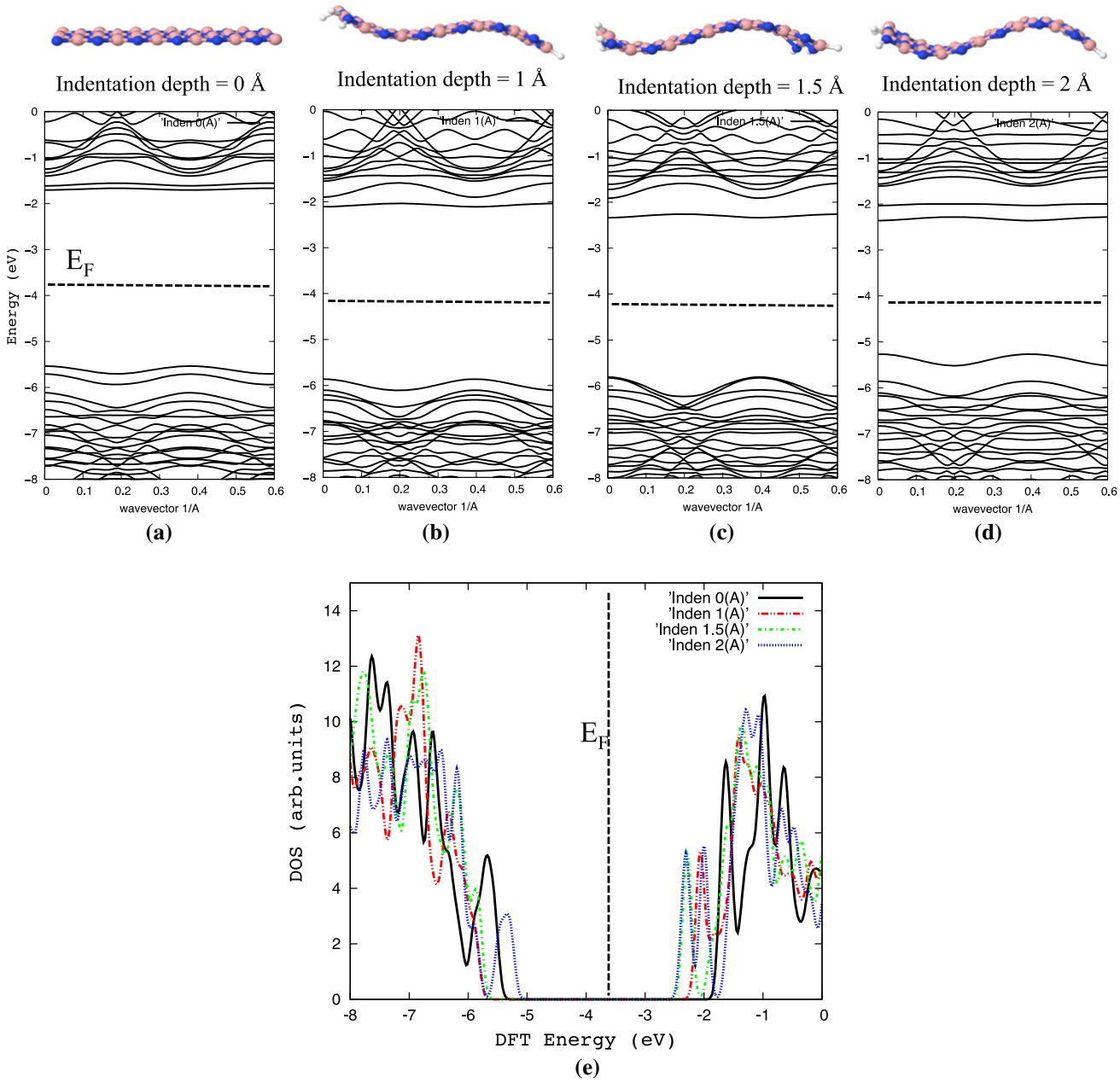

Fig. 6. The deformation sequence for sine-wave distortion of BNRs: (a) flat (unloaded) structure, (b–d) with indentation depth δ = 1.0 Å, 1.5 Å, and 2.0 Å and middle panel shows their electronic band structure for BNRs. (e) Total density of states (DOS) for a loaded structure with indentation depth of 1.0 Å, 1.5 Å, and 2.0 Å compared with a flat structure.

thus electronic properties of nanocomposites, and optical and nanoelectronic devices. Beyond boron nitride, the fundamental concepts, methods and strategies of this work may have important implications for understanding and tuning a host of several other 2D mono- and multi-layer atomic sheets (e.g. molybdenum disulfide, niobium diselenide, layered double hydroxides, etc.) used for nanoelectronics.

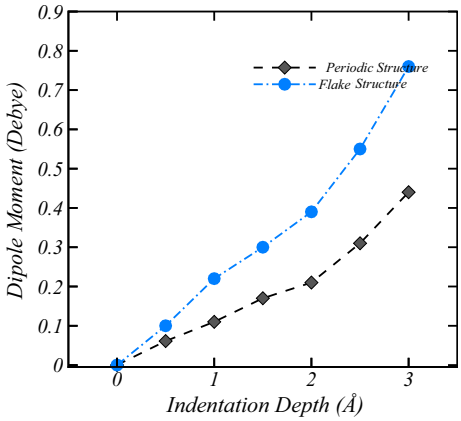

Fig. 7. Variation of the dipole moment of BNRs along the different indentation depth for periodic BNR structure and BN flake.

ACKNOWLEDGMENTS

RS and FS acknowledge the financial support from the National Science Foundation (1709051). The supercomputer machines utilized in this work were supported in part by NIH award NCRR S10RR02950 and an IBM Shared University Research (SUR).

CONFLICT OF INTEREST

The authors declare no competing financial interest.

APPENDIX

The density of states (DOS) relates to the imaginary part of summing over diagonal elements of Green's function matrix by $D(\varepsilon) = -\mathrm{Im}Tr\,G(E)/\pi$.[37,38] By substituting elemental members, DOS can be presented as:

$$D(\varepsilon) = -\frac{1}{2\pi MN}\sum_{m=1}^{M}\sum_{k_x\in FBZ}^{N}\mathrm{Im}\,G^{(m)}(K_x;E+i0^+)$$

Figure 2b shows the total DOS for our N = 7 BNRs. In our present system, each unit cell of the BNRs includes two N atoms, so the Hamiltonian would provide a 2 N × 2 N matrix in the following structure

$$G(k_x;\tau) = \begin{pmatrix} G_+^{(1)}(k_x;\tau) & 0 & 0 & \dots & 0 \\ 0 & G_-^{(1)}(k_x;\tau) & 0 & \dots & 0 \\ 0 & 0 & G_+^{(2)}(k_x;\tau) & \dots & 0 \\ \vdots & \vdots & \vdots & \ddots & \vdots \\ 0 & 0 & 0 & \cdots & G_-^{(M)}(k_x;\tau) \end{pmatrix}$$

where $G_\pm^{(m)}(k_x;\tau) = -\left\langle Tc_{\pm,k_x}^{(m)}(\tau)c_{\pm,k_x}^{(m)\dagger}(0)\right\rangle$ refers to each element of the matrix, in which T is time ordering operator and $\tau = it$. After Fourier transformation and $E = \varepsilon + i0^+$, the energy-dependent Green's function for the considered Hamiltonian becomes:

$$G(k_x;E) = \begin{pmatrix} E-\varepsilon_+^{(1)}(k_x) & 0 & 0 & \dots & 0 \\ 0 & E-\varepsilon_-^{(1)}(k_x) & 0 & \dots & 0 \\ 0 & 0 & E-\varepsilon_+^{(2)}(k_x) & \dots & 0 \\ \vdots & \vdots & \vdots & \ddots & \vdots \\ 0 & 0 & 0 & \cdots & E-\varepsilon_-^{(M)}(k_x) \end{pmatrix}^{-1}$$

REFERENCES

1. R.B. Meyer, *Phys. Rev. Lett.* 22, 918 (1969).
2. P.G. Gennes and J. Prost, *The Physics of Liquid Crystals* (Oxford: Clarendon Press, 1993).
3. A.K. Tagantsev, *Phys. Rev. B* 34, 5883 (1986).
4. N.D. Sharma, R. Maranganti, and P. Sharma, *J. Mech. Phys. Solids* 55, 2328 (2007).
5. E.J. Mele and P. Král, *Phys. Rev. Lett.* 88, 056803 (2002).
6. S.M. Nakhmanson, A. Calzolari, V. Meunier, J. Bernholc, and M. Buongiorno Nardelli, *Phys. Rev. B* 67, 235406 (2003).
7. N. Sai and E.J. Mele, *Phys. Rev. B* 68, 241405(R) (2003).
8. S.H. Mir, S. Chakraborty, P.C. Jha, J. Warna, H. Soni, P.K. Jha, and R. Ahuja, *Appl. Phy. Lett.* 109, 053903 (2016).
9. M.J. Rand and J.F. Roberts, *J. Electrochem. Soc.* 115, 423 (1968).
10. J. Lan, J.-S. Wang, C.-K. Gan, and S.-K. Chin, *Phys. Rev. B* 79, 115401 (2009).
11. K. Miyoshi, D.H. Buckley, J.J. Pouch, S.A. Alterovitz, and H.E. Sliney, *Surf. Coat. Technol.* 33, 221 (1987).
12. G. Leichtfried, *13.5 Properties of Diamond and Cubic Boron Nitride. P. Beiss, Landolt-Börnstein—Group VIII Advanced Materials and Technologies: Powder Metallurgy Data. Refractory, Hard and Intermetallic Materials*. 2A2 (Springer, Berlin, 2002), pp. 118–139. https://doi.org/10.1007/b83029, ISBN:978-3-540-42961-6.
13. J. Yu, Z. Zheng, H.C. Ong, K.Y. Wong, S. Matsumoto, and W.M. Lau, *Phys. Chem. B* 110, 21073 (2006).
14. R. Shahsavari, *ACS Appl. Mater. Interfaces* 10, 2203 (2018).
15. P.K. Jha and R.H. Soni, *Appl. Phys.* 115, 023509 (2014).
16. H. Zeng, C. Zhi, Z. Zhang, X. Wei, X. Wang, W. Guo, Y. Bando, and D. Golberg, *Nano Lett.* 10, 5049 (2010).
17. B. Roondhe, K. Prafulla, and P.K. Jha, *J. Mater. Chem. B* 6, 6796 (2018).
18. B. Roondhe, S.D. Dabhi, and P.K. Jha, *Appl. Surf. Sci.* 441, 588 (2018).
19. A. Lopez-Bezanilla, J. Huang, H. Terrones, and G. Bobby, *Nano Lett.* 11, 3267 (2011).
20. Z. Zhang and W. Guo, *Phys. Rev. B* 77, 075403 (2008).
21. C.H. Park and S.G. Louie, *Nano Lett.* 8, 2200 (2008).
22. J. Qi, X. Qian, L. Qi, J. Feng, D. Shi, and J. Li, *Nano Lett.* 12, 1224 (2012).
23. J.M. Pruneda, *Phys. Rev. B* 81, 161409 (2010).
24. S. Dutta, A.K. Manna, and S.K. Pati, *Phys. Rev. Lett.* 102, 096601 (2009).
25. X. Fan, Z. Shen, A.Q. Liu, and J.-L. Kuo, *Nanoscale* 4, 2157 (2012).
26. Z. Zhang, W. Guoa, and B.I. Yakobson, *Nanoscale* 5, 6381 (2013).
27. L. Song, L. Ci, H. Lu, P.B. Sorokin, C. Jin, J. Ni, A.G. Kvashnin, D.G. Kvashnin, J. Lou, B.I. Yakobson, and P.M. Ajayan, *Nano Lett.* 10, 3209 (2010).
28. J. Wang, F. Ma, and M. Sun, *RSC Adv.* 7, 16801 (2017).
29. H. Zheng, Z.F. Wang, T. Luo, Q.W. Shi, and J. Chen, *Phys. Rev. B* 75, 165414 (2007).
30. K. Zhao, M. Zhao, Z. Wang, and Y. Fan, *Physica E* 43, 440 (2010).
31. R.M. Ribeiro and N.M.R. Peres, *Phys. Rev. B* 83, 235312 (2011).
32. G. Kresse and J. Hafner, *Phys. Rev. B* 49, 14251 (1994).

33. G. Kresse and J. Furthmuller, *Phys. Rev. B* 54, 11169 (1996).
34. P.E. Blochl, *Phys. Rev. B* 50, 17953 (1994).
35. J.P. Perdew, K. Burke, and M. Ernzerhof, *Phys. Rev. Lett.* 77, 3865 (1996).
36. F. Shayeganfar, J. Beheshtian, and R. Shahsavari, *Langmuir* 34, 11176 (2018).
37. E.N. Economou, *Green's Functions in Quantum Physics*, 3rd ed. (Heidelberg: Springer, 2006).
38. H. Mousavi and J. Khodadadi, *Appl. Phys. A* 122, 14 (2016).